Research Article

ADVANCED PHOTONICS

Photoswitchable vibrational nanoscopy with sub-100-nm optical resolution

Jianpeng Ao,[a,†] Xiaofeng Fang,[b,†] Liyang Ma,[a] Zhijie Liu,[a] Simin Wu,[a] Changfeng Wu,[b] and Minbiao Ji[a,*]

[a]Fudan University, Key Laboratory of Micro and Nano Photonic Structures (Ministry of Education), Academy for Engineering and Technology, Department of Physics, State Key Laboratory of Surface Physics, Shanghai, China

[b]Southern University of Science and Technology, Department of Biomedical Engineering, Shenzhen, China

Abstract. Stimulated Raman scattering (SRS) microscopy has shown superior chemical resolution due to the much narrower vibrational spectral bandwidth than its fluorescence counterpart. However, breaking the diffraction-limited spatial resolution of SRS imaging is much more challenging because of the intrinsically weak scattering cross section and inert/stable nature of molecular bond vibrations. We report superresolution SRS (SR-SRS) nanoscopy based on reversible-switchable vibrational photochromic probes integrated with point spread function engineering strategy. By introducing a Gaussian-shaped ultraviolet excitation beam and a donut-shaped visible depletion beam in addition to the pump and Stokes beams, SR-SRS could reach sub-100 nm resolution on photoswitchable nanoparticles (NPs). Furthermore, NP-treated live cell imaging was demonstrated with resolution improvement by a factor of ~4. Our proof-of-principle work provides the potential for SR vibrational imaging to assist research on complex biological systems.

Keywords: stimulated Raman scattering; superresolution microscopy; vibrational imaging; photoswitching.

Received Jun. 22, 2023; revised manuscript received Aug. 24, 2023; accepted for publication Sep. 12, 2023; published online Sep. 30, 2023.

[DOI: 10.1117/1.AP.5.6.066001]

1 Introduction

Breaking the optical diffraction limit of far-field fluorescence microscopy to achieve superresolution (SR) nanoscopy has refreshed the portrait of molecular organizations and interactions in biological systems,[1–4] while the "color barrier" remains due to the intrinsically broad fluorescence spectra (~50 nm). In contrast, vibrational imaging offers superior chemical resolution and supermultiplexed imaging capability with much narrower bandwidth (~1 nm),[5–7] as demonstrated by stimulated Raman scattering (SRS) microscopy on alkyne-tagged Raman probes.[5,6] Consequently, spectral barcoding and immunostaining of 10 to 20 Raman species were realized,[6,8] holding the promise of elucidating intricate interactions in biosystems. However, conventional SRS microscopy is still restricted to diffraction-limited spatial resolution (~350 nm).[9] Thus pushing SRS beyond the diffraction limit has expected merit to bridge SR and supermultiplexing to enable molecular imaging with extended spatial and chemical resolution.

It is technically challenging to transfer the current fluorescence-based SR principles for SRS microscopy. Raman transition is hardly saturable for its weak cross section; local bond vibration is much more inert compared with electronic-state-coupled fluorescence and hence difficult to yield photobleaching or blinking properties. Despite the difficulties, extensive efforts have been made in sharpening the spatial resolution of SRS[10–14] and coherent anti-Stokes Raman scattering (CARS) microscopy.[15] The most straightforward means is to shorten the excitation wavelengths of SRS from the near-infrared to the visible range with the reduced point spread function (PSF),[10] though the method is still diffraction-limited, and the use of short wavelengths risks more phototoxicity and reduced imaging depth. Subdiffraction vibrational imaging techniques have been explored based on weak saturation and high-order nonlinearity,[11,13,15] which require much higher laser power to gain moderate resolution improvement. A recent demonstration of stimulated Raman excited fluorescence coupled with stimulated emission depletion strategy successfully broke the diffraction

*Address all correspondence to Minbiao Ji, minbiaoj@fudan.edu.cn

†These authors contributed equally to this work.

limit, but it requires strict frequency matching between vibrational and electronic transitions of specific dyes and involved more complex optical engineering for frequency modulation. In addition to the above optics-oriented methods, sample-oriented approaches, such as expansion-based SRS, have also been reported,[12,14] but the complex sample preparation is incompatible with live biological samples. Computation-based SR-SRS has also been demonstrated, taking advantage of deconvolution and deep-learning algorithms,[16] but the true optical means of SR-SRS imaging awaits more efforts for technical advances.

Inspired by photoswitchable fluorescence-based SR techniques, such as reversible switchable/saturable optical fluorescent transition (RESOLFT) nanoscopy,[17–19] here we report optical SR-SRS nanoscopy based on our previously developed photochromic Raman probes using diarylethene (DTE) derivatives with remarkable photoswitching properties in the cell-silent region with minimum background and high sensitivity due to the electronic preresonance-enhanced alkyne vibration.[20] In addition to the ordinary pump and Stokes beams for SRS signal detection, an ultraviolet (UV) activation beam of Gaussian shape and a visible depletion beam of donut shape were integrated to confine the final SRS PSF. The tested native photoswitchable probes showcased the subdiffraction imaging capability. To further characterize the best resolution of the method, synthesized nanoparticles (NPs) with a size of 18 nm were imaged both *in vitro* and in live cells to demonstrate SR-SRS with sub-100 nm resolution, with ~fourfold enhancement compared with conventional SRS. Our method holds promise to aid the development of SR-SRS imaging with the potential of vibrational supermultiplexing.

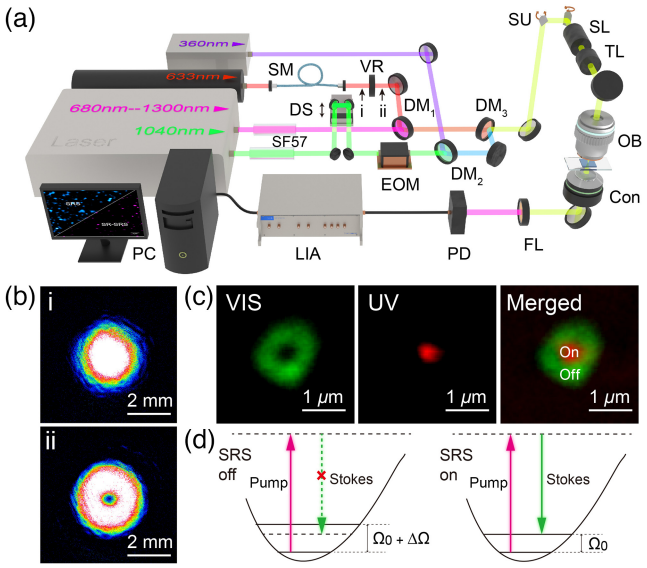

Fig. 1 Design of SR-SRS microscopy. (a) Optical layout of SR-SRS; (b) spatial profiles of the visible beam before and after VR; (c) PSF of donut-shaped visible beam and UV beam; and (d) schematic diagram of the depleted and activated SRS at the detection frequency (Ω_0) of the closed-ring isomer. Scale bar: 2 mm in (b) and 1 μm in (c). VR, vortex retarder; EOM, electro-optical modulator; LIA, lock-in amplifier; OB, objective; Con, condenser; DM, dichroic mirror; SM, single-mode fiber; PD, photodiode; F, filter; PC, personal computer; DS, delay stage; SU, scanning unit; SL, scan lens; and TL, tube lens.

2 Methods

2.1 Chemical Synthesis

Methods for chemical synthesis and characterization of DTE-Ph can be found in the previous work.[20] The synthesis of the DTE-Ph nanoparticles (DTE-Ph @ NPs) is stated below.

2 mL tetrahydrofuran (THF) solution mixture with a DTE concentration of 0.1 g/L and a poly(styrene-comaleic anhydride) (PSMA, cumene-terminated, average MW ≈ 1700, styrene content 68%, purchased from Sigma-Aldrich) concentration of 0.01 g/L was quickly added into 10 mL of water in a bath sonicator for 3 min. The solution was bubbled by nitrogen and heated to 90°C to remove THF. Then the suspension solution was filtered by a 0.2 μm filter.

2.2 SR-SRS Nanoscopy Setup

Our imaging setup was based on a conventional SRS microscope coupled with an additional visible and UV laser source and is illustrated in Fig. 1. For the SRS microscope, pulsed femtosecond laser beams from a commercial optical parametric oscillator (OPO) laser (Insight DS+, Newport, California, United States) were used as the laser source. The fixed fundamental 1040 nm laser was used as the Stokes beam, while the tunable OPO output (680 to 1300 nm) served as the pump beam. Chirped by SF57 glass rods, pulse durations of the pump and Stokes beams were stretched to ~2.3 and ~1.2 ps, respectively. The intensity of the 1040 nm Stokes beam was modulated at 1/4 of the laser pulse repetition rate ($f_0 = 80$ MHz) using an electro-optical modulator (EOM). The two pulse trains were spatially and temporally overlapped through a dichroic mirror (DM_3) and delay stage (DS), delivered into a laser scanning microscope (FV1200, Olympus), and focused onto the sample with an objective lens (Olympus, UPLSAPO60XW, NA = 1.2). The forward-going pump and Stokes beams, after passing through the samples, were collected in transmission with a high-NA condenser lens (oil immersion, 1.4 NA, Nikon). The stimulated Raman loss signal was optically filtered (CARS ET890/220, Chroma), detected by a homemade reverse-biased photodiode (PD), and demodulated with a lock-in amplifier (LIA) (HF2LI, Zurich Instruments) to feed the analog input of the microscope to form images. In order to induce the conversion of the DTE molecules, an additional HeNe laser served as the visible beam and was engineered into a donut shape with a vortex retarder (VR) (VR1-633, Lbtek), and a solid-state diode laser (UV-FN-360, Changchun New Industry Optoelectronic Technology Co., China) provided the activation UV beam. Visible and UV beams were coupled into the path of pump and Stokes beams through dichroic mirrors (DM_1 and DM_2).

All laser powers were measured after the objective lens. For experiments in Figs. 2 and 3, the Stokes laser power was 9 mW and the pump laser power was 6 mW, while the visible light is 200 μW and UV power was kept at 20 μW for SR-SRS. For the cell imaging shown in Fig. 4, the laser powers were used as $P_{\text{Stokes}} = 40$ mW and $P_{\text{pump}} = 20$ mW, $P_{\text{VIS}} = 300$ μW, and $P_{\text{UV}} = 50$ μW. Pixel dwell times were set at 40 μs. To meet the Nyquist sampling theorem, an imaging area of 20.8 μm × 20.8 μm with 800 pixels × 800 pixels was set (pixel sampling size of 26 nm).

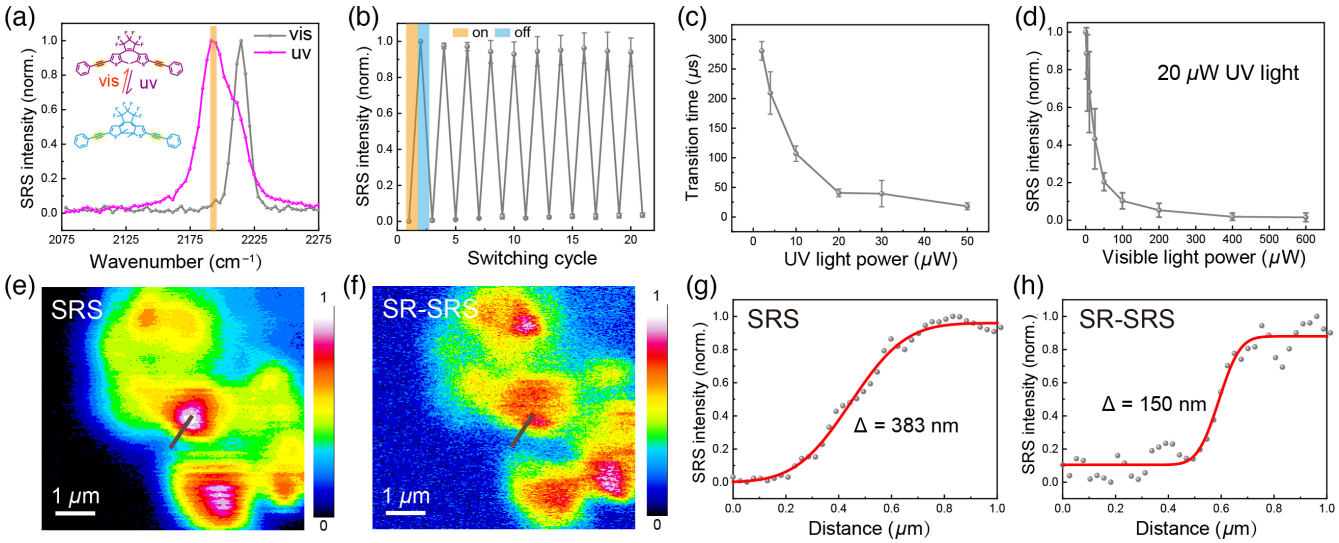

Fig. 2 Properties of photoswitchable Raman probe and SR-SRS imaging of native probe molecules. (a) SRS spectra of DTE-Ph in the open- and closed-ring isomers upon visible and UV light; (b) SRS signal of DTE-Ph acquired at the UV-induced Raman frequency (2194 cm^{-1}) shows on/off switching behavior under UV/visible pulsed irradiations; (c) relationship of on-switching transition time under different powers of the UV beam; (d) SRS signal depletion under different visible laser powers and fixed 20 μW UV power; (e) SRS and (f) SR-SRS images of the probe powder; and (g), (h) normalized intensity profiles along the line cuts in (e) and (f). Scale bar: 1 μm.

2.3 SRS Imaging of DTE-Ph @ NPs

The DTE-Ph @ NPs suspended solution (370 ppm; parts per million) was resuspended in deionized water by a 1:200 dilution. The solution is sonicated for 10 min at room temperature before being dropped onto a glass slide. When the solution is naturally dried, the slide is sandwiched by a cover glass for SRS imaging.

2.4 Cell Culturing and Imaging

Before labeling experiments, HeLa cells were cultured with a DMEM medium (Invitrogen, 11965092) supplemented with 10% FBS (Invitrogen, 16000) and 1% penicillin–streptomycin (Invitrogen, 15140) at a humidified environment at 37°C and 5% CO_2. All samples were assembled into a chamber using a homemade punched slide filled with PBS solution for imaging. In the experiment of NP treatment, cells were seeded and cultured on a glass coverslip in a 6-well plate for 24 h and then incubated with 2 ppm DTE-Ph @ NPs for 4 h. Before imaging, cells were washed with PBS 3 times.

2.5 Fourier Transform Infrared Spectroscopy

The IR spectra presented in Fig. S9 in the Supplementary Material were measured using a Bruker Fourier transform infrared (FTIR) spectrometer (Vertex 70v) equipped with a Hyperion 2000 microscope at room temperature. Before the test, DTE powder (~1 mg) was dissolved ahead of time in 0.5 mL poly(methyl methacrylate), and the mixture was spin-coated onto a quartz substrate. The incident light was focused on the coated DTE sample using a 15× IR objective, and IR radiation was collected by a liquid nitrogen cooled mercury cadmium telluride detector.

3 Results

3.1 RESOLFT-Based SR-SRS Microscopy

Typical far-field SR nanoscopy breaks the diffraction barrier by manipulating molecules into different states in the time (localization-based) or spatial (PSF engineering-based) domain.[17,21–24] Localization-based methods differentiate identical single molecules on the basis of individual stochastic behavior in time with either photobleaching or reversible blinking under wide-field illumination.[23,24] Such wide-field imaging modality is incompatible with the point-scanning-based SRS; hence we chose to realize SR-SRS by PSF engineering combined with photoswitching properties.

The optical setup of our SR-SRS was constructed by integrating a basic SRS signal detection/imaging framework with a RESOLFT focal engineering part [Fig. 1(a)]. For the conventional SRS, a fixed fundamental laser beam (1040 nm) stretched to ~1.2 ps was used as the Stokes beam, and the tunable OPO output (680 to 1300 nm, stretched to ~2.3 ps) served as the pump beam, both of which kept Gaussian-shaped intensity profiles with diffraction-limited overlapping focal spots (see Fig. S1 in the Supplementary Material). Since the photoswitchable Raman probes follow UV activation and visible quenching when imaged at the alkyne Raman band of the closed-ring isomer (~2194 cm^{-1} for DTE-Ph),[20] a Gaussian-shaped UV beam (CW solid-state diode laser, 360 nm) was used to turn on the molecules, whereas a visible donut-shaped beam (CW HeNe laser, 633 nm) was used to switch off the SRS signal to sharpen the PSF. Figure 1(b) indicates that the donut beam was converted from a Gaussian beam by a VR as verified by CCD imaging before and after the VR. In the end, the four beams were combined and overlapped through DMs to interact with samples under the laser scanning microscope. The PSF profiles of the

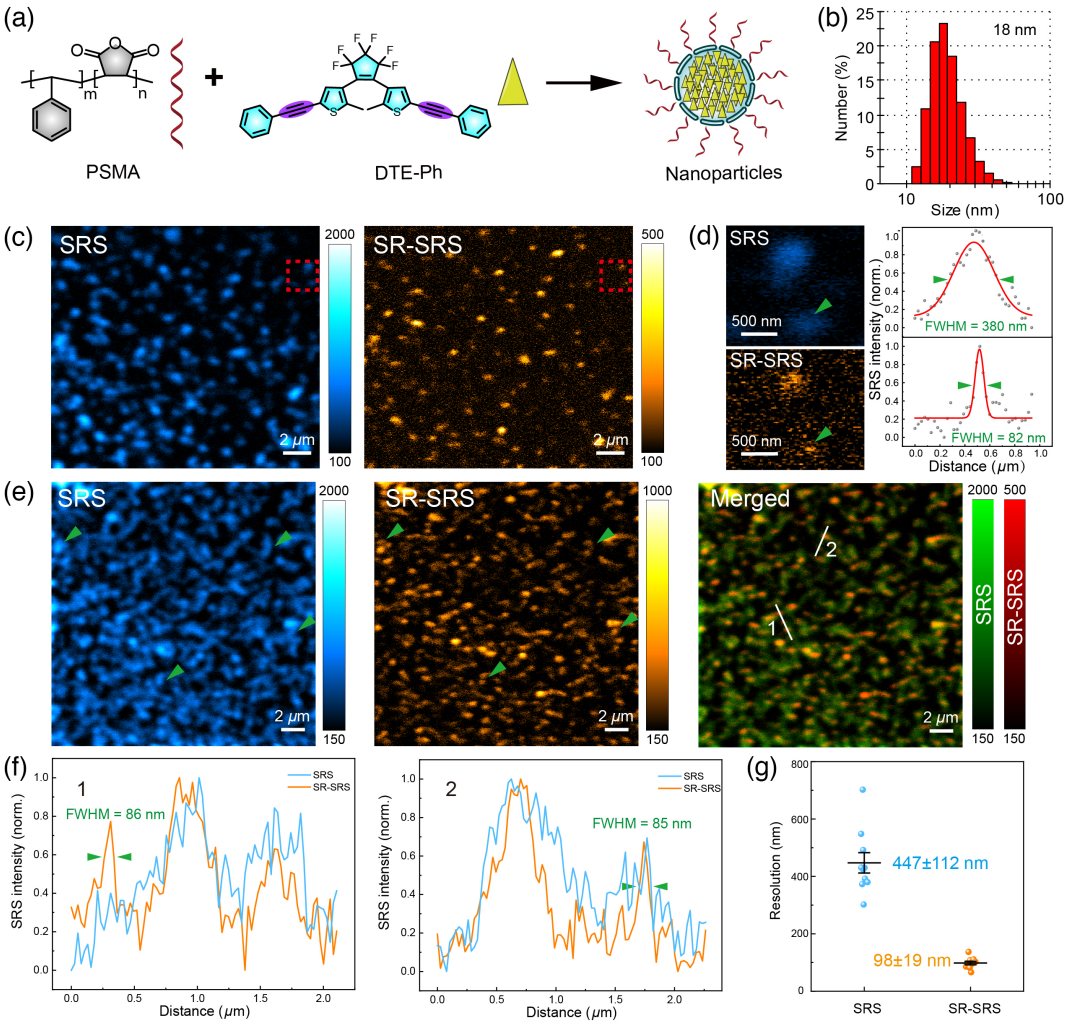

Fig. 3 SR-SRS imaging of synthesized DTE-Ph NPs. (a) Schematics of NP synthesis; (b) size distribution of NPs determined by DLS; (c) SRS and SR-SRS images of the NPs spread on glass slide; (d) zoom-in images of the labeled rectangle regions in (c) and data fitted by Gaussian function of the single dots pointed with green arrowheads; (e) SRS and SR-SRS images of the NPs; (f) intensity profile along the lines marked in (e); and (g) statistical analysis of multiple particles ($n = 10$). Scale bar: 2 μm in (c), (e) and 500 nm in (d).

visible and UV beams after the objective lens were determined by imaging the light scattering of single Au NPs [Fig. 1(c)]. Thus the working principle of SR-SRS could be clearly pictured: at the particular SRS detection frequency, only molecules at the very center of the focal spot remain in the "on-state" by continuous UV activation, whereas the peripheral molecules in the donut area are erased as they frequency-shifted to the "off-state" by visible-light-induced isomerization [Fig. 1(d)]. The competition of UV and visible spots effectively compresses the PSF of the final SRS signal, improving the spatial resolution beyond the diffraction limit.

3.2 *Reversible Photoswitching Properties of Raman Probes*

Fluorescence-based SR microscopy mostly relies on the sensitive photochemical or photophysical properties of electronic transitions in fluorescence probes, which are usually lacking in vibrational transitions, hindering Raman probes from possessing photoactive properties for SR imaging. In our previous work, we screened out two photochromic vibrational probes—DTE-TMS and DTE-Ph (see Fig. S2 in the Supplementary Material) and demonstrated reversible photoswitchable SRS imaging.[20] Here we chose to use a DTE-Ph molecule to investigate SR-SRS because of its enhanced SRS signal intensity and superior on–off ratio (~50) in the background-free spectral region, which are the keys to optimizing the spatial resolution of RESOLFT-based SR microscopy.

We first characterized the critical photoswitching properties of DTE-Ph to obtain the optimum activation and depletion parameters. The photoisomerization of DTE-Ph renders a large SRS frequency shift (~20 cm^{-1}) of the alkyne vibration, switching between the closed-ring (~2194 cm^{-1}) and the open-ring (~2214 cm^{-1}) isomers under UV/visible light irradiations [Fig. 2(a)]. Unless specifically stated, SRS detection frequency

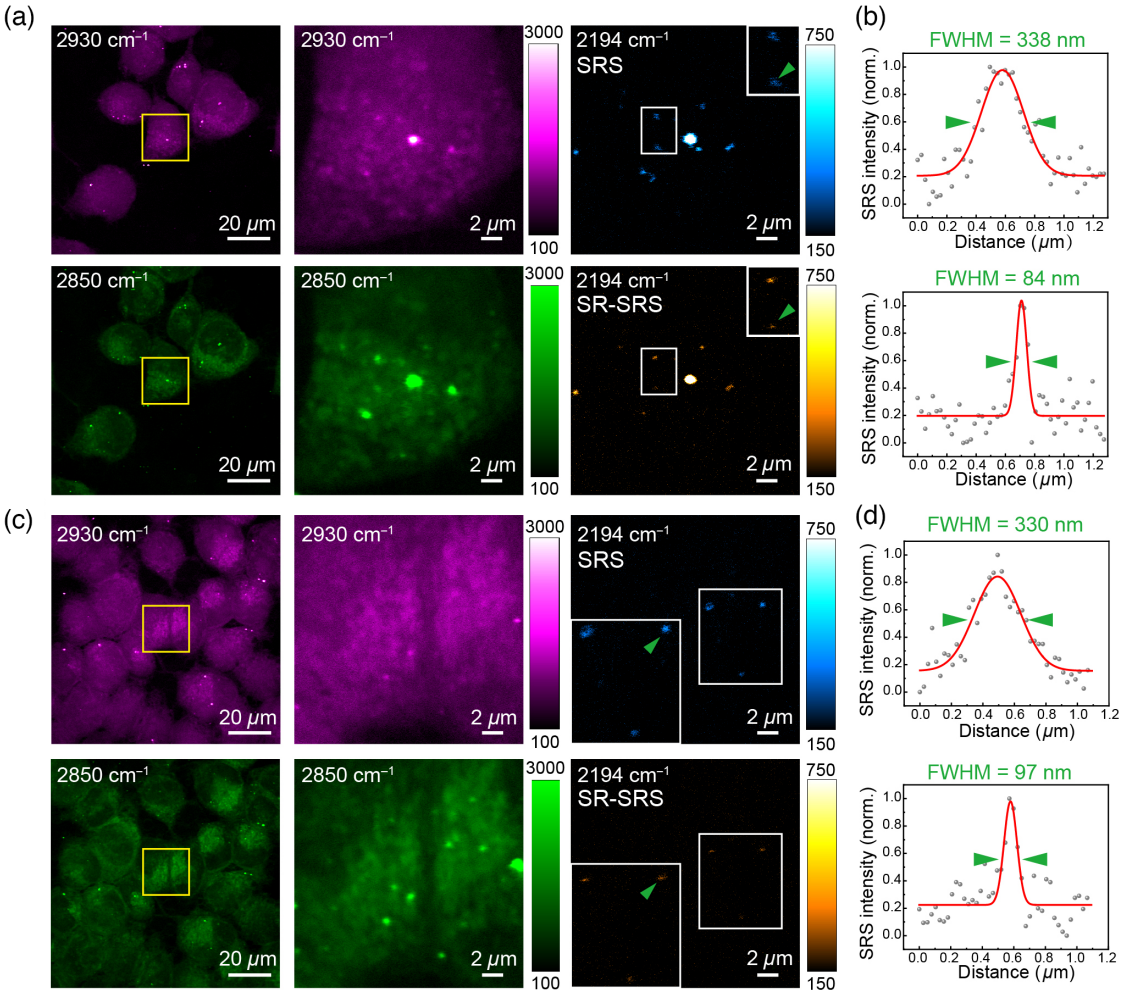

Fig. 4 SR-SRS imaging of live cells. (a), (c) SRS images of NPs treated HeLa cells at different Raman frequencies: CH_2 symmetric stretch (2850 cm^{-1}), CH_3 symmetric stretch (2930 cm^{-1}), alkyne stretches of the closed-ring (2194 cm^{-1}) isomers, and corresponding SR-SRS at the activate frequency (2194 cm^{-1}). (b), (d) Data fitted by Gaussian function of the dots pointed with green arrowheads in (a) and (b). Scale bar: 20 μm in zoom-out images and 2 μm in zoom-in images.

was kept at 2194 cm^{-1} throughout the work; hence the on/off states were defined as the closed/open-ring isomers. Figure 2(b) shows robust reversible on/off switching behavior and a high on/off ratio of the probe molecule under periodic and out-of-phase UV/visible irradiations ($n = 3$), with clear transition times during the activation and depletion processes. We measured the onset transition time under various UV doses to determine the optimum activation parameters for the laser point-scanning imaging mode. As the UV dose increased, the transition time continuously shortened till it reached a constant level (~40 μs) at the UV power of ~20 μW [Fig. 2(c), $n = 3$]. A prolonged UV irradiate dose is likely to cause irreversible photoreactions to kill the switchable capability;[25,26] thus the preferred UV activation power was set to 20 to 30 μW with a pixel dwell time of 40 μs. The depletion property of visible irradiation was characterized by measuring the SRS intensity of the probe molecules with varying visible power under a fixed UV dose (20 μW). It can be seen that visible irradiation could effectively suppress the SRS signal, and almost completely depleted it when the visible power reached above 100 μW [Fig. 2(d), $n = 9$].

3.3 SR-SRS Imaging of Native Probe Molecules

With the determined activation and depletion parameters, we then performed SR-SRS on native probe molecules in powder form. The applied laser powers of the four beams were set as 30 μW for the UV (360 nm), 200 μW for the visible (633 nm), 6 mW for the pump (845 nm), and 9 mW for the Stokes (1040 nm). A pixel dwell time of 40 μs was chosen to match the switching time. In the presence of the visible beam, the SR-SRS image showed overall reduced signal intensity compared with conventional SRS due to the compressed effective PSF, as shown in Figs. S3(a) and S3(b) in the Supplementary Material. Meanwhile, more details of the morphological features could be visualized [see arrowhead in Fig. S3(a) in the Supplementary Material]. To make a more direct comparison, the line-cut profiles were taken across the imaged region with normalized intensities [Fig. S3(c) in the Supplementary Material]. As illustrated in the shadow-colored regions of the line profiles, the conventional SRS image only depicted three broad lumps, whereas the SR-SRS image resolved a number

of much sharper peaks, indicating improved spatial resolution. For quantitative evaluation, the intensity distributions across the edges of the imaged powder were extracted and shown in Figs. 2(e) and 2(f). The data were fitted with error function $[\alpha(x) = A_1 \int_{-\infty}^{x} \exp(-t^2/x_0^2)\mathrm{d}t + A_2]$ to determine the resolution quantitatively, where A_1, A_2, and x_0 are the fitting parameters.[11,15] The lateral resolution could be calculated as the full width at half maximum (FWHM) of the Gaussian function in the fitting function $\Delta = 2\sqrt{\ln 2}x_0$ [Figs. 2(g) and 2(h)]. Although conventional SRS provided a resolution of ~380 nm, SR-SRS presented a value of ~150 nm, offering an improvement factor of ~2.5. However, this approach only offers a quick and rough estimation; it might underestimate the resolution because the physical interface of the sample might not be a true sharp step.

3.4 SR-SRS Nanoscopy of Optimized DTE-Ph NPs

To more precisely characterize the resolution of SR-SRS, the probes were synthesized into DTE-Ph @ NPs as detailed in Sec. 2. Briefly, DTE-Ph molecules were swelled by PSMA in a concentration of around 90% and formed nanoscale spherical particles [Fig. 3(a)]. The size of the DTE-Ph @ NPs in water suspension was determined by dynamic light scattering (DLS), showing an average diameter of ~18 nm [Fig. 3(b)]. The compact particle size is suited for the demonstration and characterization of SR imaging capability.

DTE-Ph @ NPs were spread onto a glass slide by evaporating a drop of NP solution at room temperature and were imaged without further processing. SRS spectroscopy verifies the same photoswitching properties of DTE-Ph @ NPs as the native probe (see Fig. S4 in the Supplementary Material). Meanwhile, we noticed a slightly increased transient absorption background in the SRS spectrum under UV irradiation. Nonetheless, such a background was not seen in the open-ring isomer upon visible-light illumination; thus the on/off ratio remained sufficient to ensure a high improvement factor of the spatial resolution.

For direct comparison, we imaged the DTE-Ph @ NPs with conventional SRS and SR-SRS, as shown in Fig. 3(c). Individual bright dots of the NPs indicated that the particles were dispersed with small amount of aggregation, well suited for quantifying the resolution. As we switched from conventional SRS to SR-SRS by coupling the UV-activation and visible-depletion beams, the imaged NPs appeared much sharper, with reduced signal intensity and particle sizes, indicating a significant increase of spatial resolution [Fig. 3(c)]. This could also be verified by comparing the imaging results of UV-only, visible-only, and UV + visible (see Fig. S5 in the Supplementary Material), showing the resolution enhancement truly originated from the combination of UV and visible beams. Single-dot analysis showed that measured NP sizes as small as ~82 nm [arrowhead in Fig. 3(d)] could be identified by FWHM fitting using Gaussian functions in the magnified areas of the SR-SRS image [red dotted rectangle in Fig. 3(c)]. Compared with the 380 nm size determined by conventional SRS of the same NP, an enhancement of the lateral resolution by a factor of ~4.6 could be reached.

We also demonstrated SR imaging in regions with more crowded particles, where dots/aggregates were often too close to be resolved in conventional SRS. In contrast, the fine features could be clearly identified in SR-SRS images, including the isolation of two nearby particles and the differentiation of multiple substructures in the aggregates [Fig. 3(e)]. More obvious distinction could be visualized in the merged image, as the dots imaged with SR-SRS (red) appeared more compact than that in conventional SRS (green). The resolution enhancement could also be clearly shown in the intensity profiles along the line cuts across particles and aggregations, as shown in Fig. 3(f) and the lines in Fig. 3(e). Unresolvable peaks in conventional SRS could now be well differentiated as multiple peaks in SR-SRS, and the sharpest peak in each profile was characterized by Gaussian function to verify the sub-100 nm resolution [see lines #1 and #2 in Fig. 3(f)]. More data for intuitive comparison of NP images may be found in Fig. S6 in the Supplementary Material. We have performed a statistical analysis of imaged particles to present the PSF size improvement [see Fig. 3(g)]; these were all the particles selected within a single image to meet the criteria of the weakest measurable signal to avoid aggregates larger than the SR PSF.

3.5 SR-SRS Imaging of Live Cells

To further demonstrate the potential of SR-SRS nanoscopy for biological imaging, we fed HeLa cells with the DTE-Ph @ NPs as detailed in Sec. 2, on account of the cellular uptake of NPs via endocytosis with low toxicity.[27,28] The treated live HeLa cells were imaged with both conventional and SR-SRS modalities. In Fig. 4(a), we first checked the cellular regions using rapid-scanning mode in the C–H vibrational band for lipid/protein imaging (2850 cm^{-1} for CH_2 and 2930 cm^{-1} for CH_3) to locate the cells of potential interest under low magnification. Then the field of view was zoomed-in to observe finer intracellular features, including subcellular compartments and lipid droplets, as shown in the C–H channels, as well as the endocytosed NPs imaged in the alkyne channel (2194 cm^{-1}) without any background inference from the cells. To meet the Nyquist sampling theorem, an imaging area of 20.8 μm × 20.8 μm with 800 pixels × 800 pixels was set (pixel sampling size of 26 nm). From the SRS images of NPs and cells, we can see the dots tend to stay in cytoplasm with sparse distribution because of the low uptake concentration, offering the basis of resolution quantification for live cell imaging. The sizes of the smallest dots found inside cells matched well with the *in vitro* results [Figs. 3(d) and 4(b)]. The FWHM of the dot in conventional SRS image was analyzed to be ~338 nm, in contrast to that of ~84 nm in the corresponding SR-SRS image, proving the ~fourfold enhancement of resolution of our system [Fig. 4(b)]. Similar results could be seen repeatedly in different cells with sub-100 nm resolution [Figs. 4(c) and 4(d)]. Figure S7 in the Supplementary Material shows the statistical results of the resolution measurement.

4 Discussion

Biological research usually favors optical imaging methods because of their nondestructive nature, which is compatible with the dynamic observation of living systems, in contrast to destructive techniques, such as cryogenic electron microscopy, while the relatively low spatial resolution limits the optical study of structural details. Improving the resolution of optical microscopy has long been pursued; although it has shown numerous successes in SR fluorescence nanoscopy, it remains challenging for vibrational imaging to reach the subdiffraction limit. SRS microscopy offers high chemical specificity and multiplexity by probing molecular bond vibrations.[5,6] In addition to the initial

aims of label-free chemical imaging,[29–32] SRS has recently branched into a unique labeling imaging technique.[20,33–38] Alkyne-based Raman probes showed remarkable advantages of high sensitivity, freedom from cellular background, and narrow spectral linewidth.[38] We have stepped further to engineer photoswitchable Raman probes by coupling alkyne groups with photochromic DTE molecules.[20] Compared with other forms of photoswitchable Raman probes,[35,36] DTE-alkyne molecules showed superior signal intensity, photostability, fatigue resistance, and minimum background. These properties are crucial for SR-SRS imaging under RESOLFT geometry, especially for pushing forward the spatial resolution, where the major limiting factors include the reduced signal-to-noise ratio (SNR) due to the smaller and smaller PSF, and the nonswitchable background (e.g., cell spectra in the fingerprint region) may effectively limit the on/off ratio.

Thanks to the superb photoswitching properties of DTE-Ph probe, we have reached down to sub-100 nm resolution with low-power UV and visible beams, in contrast to other types of optics-oriented SR-SRS with moderate resolution improvement.[11,13] Comparing with sample-oriented SR-SRS methods,[12,14] our approach does not require complex sample processing; hence, it is compatible with live bioimaging. With functional targeting modification, the SR modality could be reached in organelle structure imaging to map subcellular architectures and study their biological behaviors, such as mitochondria–mitochondria contact and endoplasmic reticulum modulation. SR-SRS may also be integrated with immunohistochemical labeling to resolve finer structures with higher specificity. Note that ideally SR supermultiplex vibrational imaging should be achieved with the current experimental design. However, engineering a series of high-quality photoswitchable Raman probes becomes the technical bottleneck to realizing this goal. Moreover, as can be seen in the quantitative results [Figs. 2(g), 2(h), 3(d), 3(f), and 4(b), 4(d)], the SNR of SR-SRS may be the ultimate limit for further improvement of spatial resolution; yet it is inappropriate to increase the power of pump and Stokes beams because they are more likely to induce photocyclization through the two-photon absorption effect (see Fig. S8 in the Supplementary Material). Apart from the experimental improvements, image denoising might be an additional choice to increase the SNR, owing to the rapid development of deep-learning algorithms.[39–42] Furthermore, as another powerful vibration spectroscopy, IR absorption coupled with photochromic probes may demonstrate interesting photoswitching capability, as shown in Fig. S9 in the Supplementary Material and could be potentially realized for SR vibrational imaging as well.

In conclusion, we have constructed SR-SRS nanoscopy based on photoswitchable probes combined with RESOLFT strategy and demonstrated improved resolution down to sub-100 nm. Both *in vitro* and live-cell imaging results were consistent with the enhancement factor of ∼4 compared with conventional SRS. Our methods may be extended to achieve SR supermultiplex vibrational imaging with further developments of photoswitchable Raman probes.

Data Availability

The data that support the findings of this study are provided in the Supplementary Material and are available from the corresponding author upon request.

Author Contributions

J.A. engineered the SR-SRS light path, performed the SRS data, biological studies and analyzed the data; X.F. performed the chemical synthesis and the DLS analysis; M.J. and C.W. conceived the concept. J.A., X.F., C.W., and M.J. designed the experiments and wrote the paper with input from all authors.

Acknowledgments

We would like to thank P. Wang for the kind provision of SM fiber and H. Yan for the support of FTIR measurement. M. Ji would like to acknowledge the financial support from the National Key Research and Development Program of China (Grant No. 2021YFF0502900), the National Natural Science Foundation of China (Grant Nos. 61975033 and 81771930), the Shanghai Municipal Science and Technology Major Project (Grant Nos. 2017SHZDZX01 and 2018SHZDZX01), and ZJLab. C. Wu would like to acknowledge the financial support from the Shenzhen Science and Technology Innovation Commission (Grant No. KQTD20170810111314625) and the National Key Research and Development Program of China (Grant No. 2018YFB0407200).

References

1. S. W. Hell, "Toward fluorescence nanoscopy," *Nat. Biotechnol.* **21**(11), 1347–1355 (2003).
2. S. W. Hell, "Far-field optical nanoscopy," *Science* **316**(5828), 1153–1158 (2007).
3. S. W. Hell, "Microscopy and its focal switch," *Nat. Methods* **6**(1), 24–32 (2009).
4. B. Huang, H. Babcock, and X. Zhuang, "Breaking the diffraction barrier: super-resolution imaging of cells," *Cell* **143**(7), 1047–1058 (2010).
5. L. Wei et al., "Super-multiplex vibrational imaging," *Nature* **544**(7651), 465–470 (2017).
6. L. Shi et al., "Highly-multiplexed volumetric mapping with Raman dye imaging and tissue clearing," *Nat. Biotechnol.* **40**(3), 364–373 (2021).
7. W. Min et al., "Coherent nonlinear optical imaging: beyond fluorescence microscopy," *Annu. Rev. Phys. Chem.* **62**(1), 507–530 (2011).
8. F. Hu et al., "Supermultiplexed optical imaging and barcoding with engineered polyynes," *Nat. Methods* **15**(3), 194–200 (2018).
9. J. Qi et al., "Boosting fluorescence-photoacoustic-Raman properties in one fluorophore for precise cancer surgery," *Chem* **5**(10), 2657–2677 (2019).
10. Y. Bi et al., "Near-resonance enhanced label-free stimulated Raman scattering microscopy with spatial resolution near 130 nm," *Light Sci. Appl.* **7**(1), 81 (2018).
11. L. Gong et al., "Saturated stimulated-raman-scattering microscopy for far-field superresolution vibrational imaging," *Phys. Rev. Appl.* **11**(3), 034041 (2019).
12. C. Qian et al., "Super-resolution label-free volumetric vibrational imaging," *Nat. Commun.* **12**(1), 3648 (2021).
13. H. Xiong et al., "Super-resolution vibrational microscopy by stimulated Raman excited fluorescence," *Light Sci. Appl.* **10**(1), 87 (2021).
14. L. Shi et al., "Super-resolution vibrational imaging using expansion stimulated Raman scattering microscopy," *Adv. Sci.* **9**(20), e2200315 (2022).
15. L. Gong et al., "Higher-order coherent anti-Stokes Raman scattering microscopy realizes label-free super-resolution vibrational imaging," *Nat. Photonics* **14**(2), 115–122 (2019).
16. H. Jang et al., "Super-resolution SRS microscopy with A-PoD," *Nat. Methods* **20**(3), 448–458 (2023).

17. M. Hofmann et al., "Breaking the diffraction barrier in fluorescence microscopy at low light intensities by using reversibly photoswitchable proteins," *Proc. Natl. Acad. Sci. U. S. A.* **102**(49), 17565–17569 (2005).
18. S. Wang et al., "GMars-Q enables long-term live-cell parallelized reversible saturable optical fluorescence transitions nanoscopy," *ACS Nano* **10**(10), 9136–9144 (2016).
19. F. Pennacchietti et al., "Fast reversibly photoswitching red fluorescent proteins for live-cell RESOLFT nanoscopy," *Nat. Methods* **15**(8), 601–604 (2018).
20. J. Ao et al., "Switchable stimulated Raman scattering microscopy with photochromic vibrational probes," *Nat. Commun.* **12**(1), 3089 (2021).
21. T. A. Klar et al., "Fluorescence microscopy with diffraction resolution barrier broken by stimulated emission," *Proc. Natl. Acad. Sci. U. S. A.* **97**(15), 8206–8210 (2000).
22. M. G. Gustafsson, "Nonlinear structured-illumination microscopy: wide-field fluorescence imaging with theoretically unlimited resolution," *Proc. Natl. Acad. Sci. U. S. A.* **102**(37), 13081–13086 (2005).
23. E. Betzig et al., "Imaging intracellular fluorescent proteins at nanometer resolution," *Science* **313**(5793), 1642–1645 (2006).
24. M. J. Rust, M. Bates, and X. Zhuang, "Sub-diffraction-limit imaging by stochastic optical reconstruction microscopy (STORM)," *Nat. Methods* **3**(10), 793–796 (2006).
25. M. Irie, "Diarylethenes for memories and switches," *Chem. Rev.* **100**(5), 1685–1716 (2000).
26. M. Irie et al., "Photochromism of diarylethene molecules and crystals: memories, switches, and actuators," *Chem. Rev.* **114**(24), 12174–12277 (2014).
27. X. Fang et al., "Multicolor photo-crosslinkable AIEgens toward compact nanodots for subcellular imaging and STED nanoscopy," *Small* **13**(41), 1702128 (2017).
28. D. Li et al., "AIE nanoparticles with high stimulated emission depletion efficiency and photobleaching resistance for long-term super-resolution bioimaging," *Adv. Mater.* **29**(43), 1703643 (2017).
29. C. W. Freudiger et al., "Label-free biomedical imaging with high sensitivity by stimulated Raman scattering microscopy," *Science* **322**(5909), 1857–1861 (2008).
30. M. Ji et al., "Rapid, label-free detection of brain tumors with stimulated Raman scattering microscopy," *Sci. Transl. Med.* **5**(201), 201ra119 (2013).
31. J. X. Cheng and X. S. Xie, "Vibrational spectroscopic imaging of living systems: an emerging platform for biology and medicine," *Science* **350**(6264), aaa8870 (2015).
32. Q. Cheng et al., "Operando and three-dimensional visualization of anion depletion and lithium growth by stimulated Raman scattering microscopy," *Nat. Commun.* **9**(1), 2942 (2018).
33. H. Xiong et al., "Stimulated Raman excited fluorescence spectroscopy and imaging," *Nat. Photonics* **13**(6), 412–417 (2019).
34. C. Chen et al., "Multiplexed live-cell profiling with Raman probes," *Nat. Commun.* **12**(1), 3405 (2021).
35. D. Lee et al., "Toward photoswitchable electronic pre-resonance stimulated Raman probes," *J. Chem. Phys.* **154**(13), 135102 (2021).
36. J. Shou and Y. Ozeki, "Photoswitchable stimulated Raman scattering spectroscopy and microscopy," *Opt. Lett.* **46**(9), 2176–2179 (2021).
37. Y. Miao et al., "9-Cyanopyronin probe palette for super-multiplexed vibrational imaging," *Nat. Commun.* **12**(1), 4518 (2021).
38. L. Wei et al., "Live-cell imaging of alkyne-tagged small biomolecules by stimulated Raman scattering," *Nat. Methods* **11**(4), 410–412 (2014).
39. B. Manifold et al., "Denoising of stimulated Raman scattering microscopy images via deep learning," *Biomed. Opt. Express* **10**(8), 3860–3874 (2019).
40. B. Manifold et al., "Versatile deep learning architecture for classification and label-free prediction of hyperspectral images," *Nat. Mach. Intell.* **3**(4), 306–315 (2021).
41. Z. Liu et al., "Instant diagnosis of gastroscopic biopsy via deep-learned single-shot femtosecond stimulated Raman histology," *Nat. Commun.* **13**(1), 4050 (2022).
42. J. Ao et al., "Stimulated Raman scattering microscopy enables Gleason scoring of prostate core needle biopsy by a convolutional neural network," *Cancer Res.* **83**(4), 641–651 (2023).

Jianpeng Ao received his PhD in physics from Fudan University, Shanghai, China, in 2023. His research mainly focuses on the technical innovation and application of nonlinear vibrational imaging.

Xiaofeng Fang received his PhD from the School of Electronic Science and Engineering at Jilin University in 2017. He continued his research as a postdoc at the Southern University of Science and Technology from 2017 to 2019. Currently, he is an assistant professor in the Department of Biomedical Engineering at the Southern University of Science and Technology. His research interests include the design, synthesis, and biomedical applications of organic functional materials.

Liyang Ma received his bachelor's degree in physics from Shandong University, Shandong, China, in 2021. He is currently a PhD candidate in the Department of Physics, Fudan University, Shanghai, China. His research mainly focuses on the biomedical applications of SRS microscopy.

Zhijie Liu received his bachelor's degree in physics from Wuhan University of Technology, Wuhan, China, in 2019. He is currently a PhD candidate in the Department of Physics, Fudan University, Shanghai, China. His research mainly focuses on deep-learning-based imaging processing.

Simin Wu received her PhD in physics from Fudan University, Shanghai, China, in 2023. She is interested in studying fundamental sciences in innovative materials via pump–probe spectroscopy.

Changfeng Wu received his PhD from the Department of Chemistry at Clemson University. He is currently a professor and associate chair in the Department of Biomedical Engineering at the Southern University of Science and Technology. His research is focused on the development of fluorescent probes for SR imaging, biosensing, and nanomedicine.

Minbiao Ji received his PhD from the Department of Physics at Stanford University. He is currently a professor in the Department of Physics at Fudan University. His research is focused on using nonlinear optical spectroscopy and microscopy to study chemical physics, material sciences, and biomedical problems.